TESCAN

TESCAN micro-CT solutions for energy storage materials research

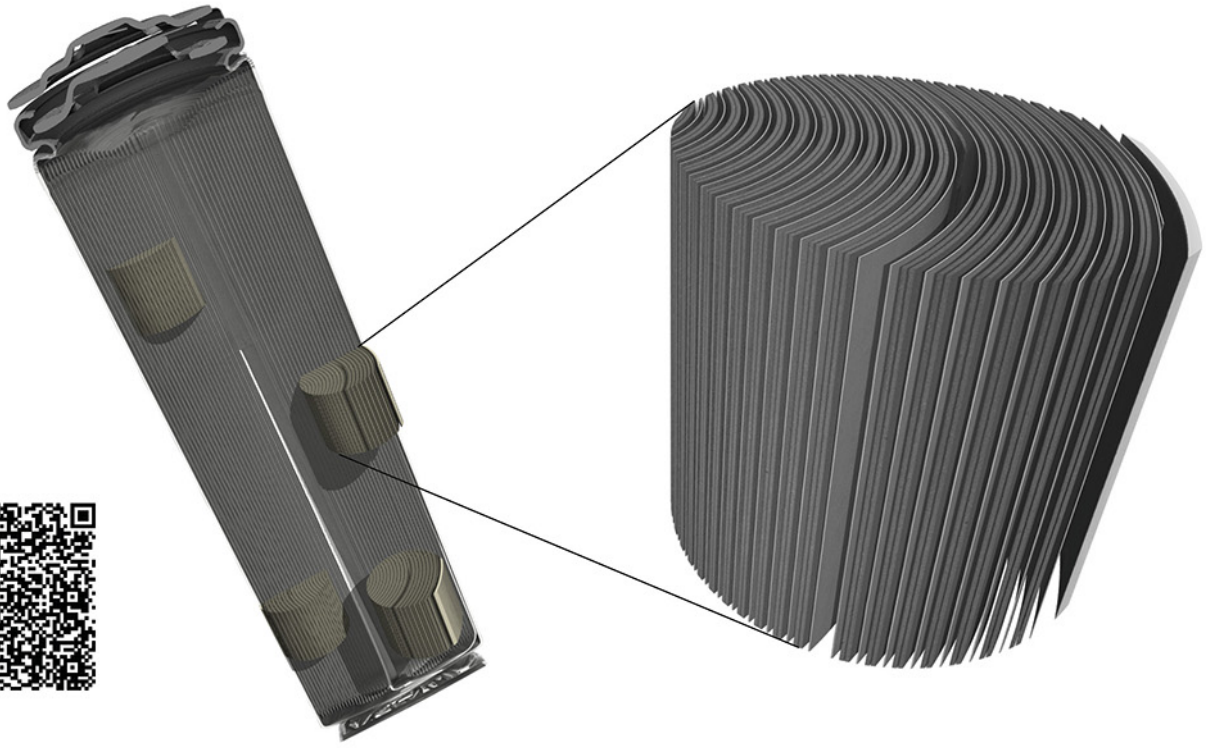

TESCAN UniTOM XL

- ✓ Multi-scale non-destructive 3D imaging optimized to maximize throughput and contrast
- ✓ Fast scanning and high sample throughput with temporal resolutions below 10 seconds
- ✓ Wide array of samples types
- ✓ Enables dynamic tomography and *in-situ* experiments
- ✓ Dynamic screening for synchrotron beamtime
- ✓ Modular and open system with unmatched flexibility for research

Click and find out more

ADVANCED ENERGY MATERIALS
www.advenergymat.de

Data-Driven Safety Risk Prediction of Lithium-Ion Battery

*Yikai Jia, Jiani Li, Chunhao Yuan, Xiang Gao, Weiran Yao, Minwoo Lee, and Jun Xu**

Inevitable safety issues have pushed battery engineers to become more conservative in battery system design; however, battery-involved accidents still frequently are reported in headlines. Identifying, understanding, and predicting safety risks have become priorities to further accelerate technology and industry development. However, diverse loading scenarios, significantly varied stress-induced short circuit mechanisms, and highly coupled mechanical–electrochemical safety behaviors have remained grand challenges. Herein, the safety risk is termed as the probability of the mechanical triggering of an internal short circuit, to reflect the safety related behaviors of lithium-ion batteries. Based on a mechanical model and experimental results, a sufficient dataset is generated consisting of strain states and their corresponding safety risks, covering both cylindrical and pouch cells, various states of charges, and loading conditions. Machine-learning tools combined with the established finite element mechanical model are applied to predict the safety risks of the cells. The results achieve a high level of accuracy on the test data (the relative error of the average short circuit prediction deviation is less than 6.2%.). This work underpins the safety risk concept and highlights the promise of physics combined with data-driven modeling methodology to predict the safety behaviors of energy storage systems.

1. Introduction

Lithium-ion batteries (LIBs) are playing increasingly important roles to promote the mobility of current society. The energy density of the LIBs has been improved significantly, along with superior cyclability and low cost. However, battery safety becomes an important factor hindering people from adopting LIBs as power sources in various scenarios. Understanding the fundamental mechanism of the LIB safety behavior would further unlock new opportunities in battery design, application, and monitoring. For example, battery suppliers may have bolder choices for high-energy-density electrode materials[1] and electrolytes.[2] Having a confident understanding of LIB safety risks also grants vehicle original equipment manufacturers (OEMs) a more extensive design space and reduces redundant protective parts,[3] which can improve the safety level and reduce the curb weights of the electric vehicles simultaneously.

Safety issues of LIBs are usually initiated from an internal short circuit (ISC).[4] The short circuit generates heat and increases the temperature, which triggers future related decomposition reactions (electrodes and electrolyte) and the phase changes (separators, collectors).[5] These complicated physiochemical changes finally lead to thermal runaway (TR) and fatal fire/explosion consequences of the batteries.[6] Mechanical abuses (excessive deformation or punctuation),[7] electrical abuses (overcharging or over-discharging),[8] and thermal abuses (overheating)[9] are three major reasons that lead to the ISC. Among them, mechanical stress stems from the external mechanical abusive loading is one of the most important and ultimate direct causations for the ISC.

Various typical mechanical abusive tests have been designed, including compression,[7c,10] indentation,[7a,c,11] bending,[7a,11c,d] and nail penetration[4b,12] to evaluate the battery safety behaviors. The mechanical and electrochemical behaviors of the batteries were characterized by recorded loading forces, open-circuit voltages, and surface temperatures in time history.[10b] Generally, the ISC is determined by the voltage drop due to the consumption of the battery capacity by joule heat.[4b] With the help of capable equipment, for example, high-speed X-ray imaging, many details of the mechanisms of TR inside cells were further revealed.[13] Considering the safety issues as well as time- and cost-effectiveness, multiphysics finite element (FE) models of batteries were established and validated to provide a reasonable description of force responses, deformation, stress field, and strain field.[7d,e,11c,d,14] The core part of such a multiphysics model is to bridge the mechanical deformation of the battery component materials with the triggering of the ISC.[11d] Pioneering work proposed either strain-[11b] or

Y. Jia, J. Li, C. Yuan, X. Gao, Prof. J. Xu
Department of Mechanical Engineering and Engineering Science
The University of North Carolina at Charlotte
Charlotte, NC 28223, USA
E-mail: jun.xu@uncc.edu
Y. Jia, J. Li, C. Yuan, X. Gao, Prof. J. Xu
Vehicle Energy & Safety Laboratory (VESL)
North Carolina Motorsports and Automotive Research Center
The University of North Carolina at Charlotte
Charlotte, NC 28223, USA
W. Yao
Department of Civil and Environmental Engineering
Carnegie Mellon University
Pittsburgh, PA 15289, USA
Prof. M. Lee
Department of Computer Science
The University of North Carolina at Charlotte
Charlotte, NC 28223, USA
The ORCID identification number(s) for the author(s) of this article can be found under https://doi.org/10.1002/aenm.202003868.

DOI: 10.1002/aenm.202003868

stress-based[11c,14b] failure criteria to indicate the boundary of ISC for a cell upon external mechanical loading. However, the results are still not satisfactory due to the following reasons: 1) An LIB cell contains multiple layers of the cathode, anode, and separator with drastically different material properties. Therefore, the stress and strain distributions throughout the cell are highly complicated such that the generalization of the model is limited; and 2) due to the stochastic nature of the complicated battery cell in material and electrochemical properties as well as possible assembling defects, the triggering of ISC should be a "probability", rather than a deterministic criterion.

To enhance the efficiency and the accuracy of the FE model, the emerging machine learning (ML) methodology was used to assist the battery safety evaluation and design.[15] Recently, Li et al. demonstrated a date-driven safety envelope predicted by several typical classifications and regression ML algorithms, including artificial neural networks and support vector machines (SVM).[16] The training samples were generated from a detailed FE model developed based on several material tests and cell tests. This method overcomes the limitation of computational sources. Apart from the prediction of ISC based on mechanical features, Naha et al. develop an online ISC detection using a Random Forests classifier.[15a] The training features are obtained from battery current and voltage data. Attia et al. and Severson et al. developed data-driven models that can accurately predict the cycle life using early-cycle data.[15c,17] The good performance stemmed from their understanding of the capacity degradation mechanism of the selected cells.[15c,17] The models greatly reduced the calculation and experimental time as well.

Nevertheless, most of the current research work using the data-driven concept and ML algorithms to solve the nonlinear and multiphysics battery safety and capacity problems is confined to certain scenarios/battery formats with limited generality. Specifically, to have an appropriately large database as training sets, either a large number of experiments or high-fidelity computational simulations should be conducted for only one specific scenario, which is time- and cost-consuming.[18]

In this work, we develop data-driven models that can accurately predict the safety risk of the LIBs induced by mechanical stress. Here, the safety risk is defined as the possibility of the triggering of the ISC under a given mechanically loading condition. Support vector regression (SVR) with radial basis function (RBF) kernel is used to predict the ISC risk based on the strain state. To accurately describe the mechanical behavior and achieve the strain states under different loading conditions, we construct a numerical computational model based on the representative volume element (RVE) perspective. The RVE-based model can achieve balance between computation cost and accuracy.[19] More importantly, based on the RVE method, various kinds of combinations of cell component layers can be represented by the same unified representative element. Therefore, the developed mechanical model can describe various types of cells. Based on the validated FE model and experimental statistics, we generate a dataset of 3150 cases (2320 for the cylindrical cell and 830 for the pouch cell) ranging from 0% SOC to 60% SOC. The safety risk prediction high-level performance of the SVR predictors is indicated by various testing cases and scenarios. The coefficient of determination R^2 of the predicted ISC risk-displacement function is large than 0.90 throughout the entire mechanical strain evolution process. The relative error of the average ISC prediction deviation is less than 6.2%. These results demonstrate the power of the experiment characterization, numerical modeling, and data-driven modeling to predict the safety risks of the energy storage systems in the future.

2. Results and Discussion

2.1. Data Generation

To validate the methodology, we selected two common types of commercially used LIBs in this study, that is, cylindrical cell and pouch cell. The cylindrical cell is a type of 18 650 cell with NCA cathode and graphite anode widely used in electric vehicles. The size is 18 mm (diameter) × 65 mm (length). The pouch cells with LCO cathode and graphite anode are widely used in cellphones and computers. The dimension is 82 mm × 63 mm × 4.4 mm. Generally, a LIB cell consists of a battery casing, a winding structure jellyroll, and some other minor electrical and structural parts (Tables S1 and S2, Supporting Information).

The LIB mechanical models are developed based on the RVE method to ensure generality and calculation efficiency. For cylindrical cells, the RVE model of the jellyroll consists of two layers of the anode, two layers of the cathode, and four layers of the separator (**Figure 1**a). An orthotropic crushable foam material model is used for these three component materials. The material properties of the jellyroll are obtained from material tests. The yield curves in the *ZZ*, and *XX*/*YY* directions are obtained from the out-of-plane compression (Figure 1b)[11c] and in-plane tension tests (Figure 1c).[7b,20] As such, the RVE model can calculate the equivalent stress–strain curve in all three directions (Figure 1d). Then, the detailed RVE can be represented by a homogenized equivalent element. The equivalent material properties are used to develop cell models. Here, a transversely isotropic crushable foam material model is used to develop the homogenized equivalent element. Also, the steel shell of the cylindrical cells with a thickness of 0.012 mm is considered. Johnson–Cook model is used to describe the elasto-plastic behavior of the shell.[20b] All the other trivial mechanical parts, such as the pressure release mechanism, are ignored. Similarly, for the pouch cell, the jellyroll is modeled in the same way, and the material properties are taken directly from our previous work.[4d] The pouch cell casing is ignored here due to its low stiffness and thin thickness (about 0.1 mm, at least an order of magnitude smaller than the thickness of the battery).[21]

To validate the mechanical models and generate a sufficient dataset, we conducted mechanical tests of two types of testing samples, including stacked-layer samples and single-cell samples. Representative mechanical loading conditions, including compression, indentation, and bending, were selected (Figure S1, Supporting Information). The stacked-layer samples were used to validated the mechanical RVE model and to generate the training dataset of jellyroll (Figure S2a, Supporting Information). For cylindrical cell stacks (32 layers), we conducted indentations in the axial direction (**Figure 2**a,b). For pouch cell stacks (24 layers), sphere indentation tests with four sizes were designed (Figure 2c).

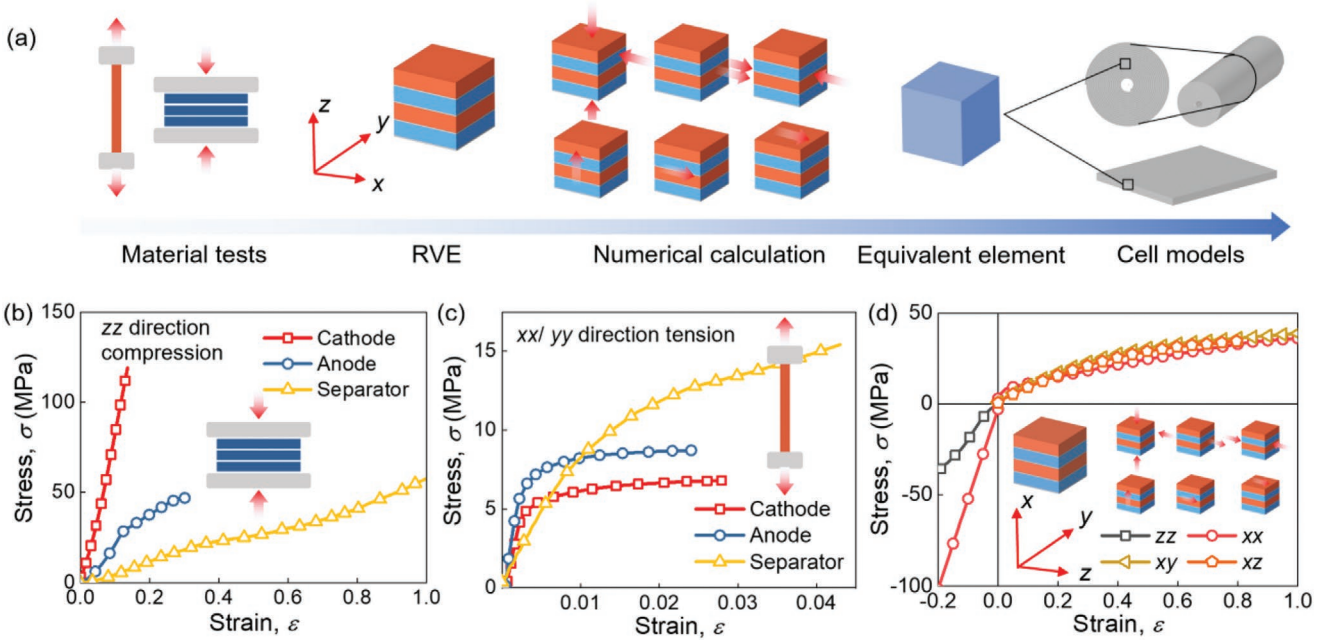

Figure 1. FE modeling methods of cells. a) Mechanical modeling processes, and used testing curves of cell constituents at b) the ZZ direction and c) XX/YY direction. d) Equivalent stress–strain curves calculated from the RVE model.

The single-cell samples were mainly used to validate the cell mechanical model to generate the testing dataset and part of the training dataset (cross template prediction among loading conditions). The single-cell samples are prepared by a cycler. The cells were fully discharged and then charged to the target state of charge (SOC) = 0.3 and 0.6, respectively. For cylindrical cells, six loading conditions were designed, including 0%- and 50%-offset compression (Figure 2d,e), 0- and 45-degree indentation (Figure 2f,g), as well as 50 mm- and 40 mm-span three-point bending conditions (Figure 2h,i). For pouch cells, out-of-plane compression and 20 mm-radius sphere indentation were designed (Figure 2j,k). All experiments were repeated five times to ensure repeatability (**Figure 3**a). The FE model accurately predicts the mechanical response at various conditions (Figure 2). Note that even if some points in the force–displacement curves have some discrepancy to the testing data, the effect on the overall accuracy of predicted safety risk is limited. Because in this study, the ML model is used to predict if the short circuit battery occurs (i.e., short circuit possibility) at a specific loading condition (deformation/strain). Thus, the training samples (points in the force–displacement curves) within the vicinity of the ISC triggering point (e.g., 5–7 mm in Figure 3, short circuit possibility Y increase from 0 to 1) weigh much more in the output Y. Thus, for the data samples in the early stage, for example, Y is zero (or close to zero), the deviation in load-displacement affects the results little.

Considering nonlinearity, complexity, and uncertainty of the safety behaviors of LIBs, the safety risk Y is defined as the probability of the triggering of ISC. According to experimental results, ISC is triggered when the loading force reaches a specific value (Figure 3a), defined as the short circuit force F_{ISC} here. F_{ISC} distribute within a value domain. Thus, we suppose F_{ISC} follows a 1D Gauss distribution, $F_{\mathrm{ISC}} \approx N(\mu, \sigma^2)$. The two parameters, that is, the mean ISC force μ and the variance σ^2, of the used gaussian possibility density distribution function, are calculated from a group of measured ISC forces:

$$\mu = \frac{1}{n}\sum_{i=1}^{n} F_{\mathrm{ISC},i} \tag{1}$$

and variance σ^2 is calculated by

$$\sigma^2 = \frac{1}{n}\sum_{i=1}^{n} (F_{\mathrm{ISC},i} - \mu)^2 \tag{2}$$

Then, the ISC triggering possibility under each loading force can be obtained by taking the integral of probability density function:

$$Y = k(F) = P(F_{\mathrm{ISC}} < F) = \int_0^F \frac{1}{\sigma\sqrt{2\pi}} e^{-\frac{(F-\mu)^2}{2\sigma^2}} \mathrm{d}F \tag{3}$$

We also have the mapping g: $s \rightarrow F$, where s is loading displacement. Thus, safety risk can be expressed by the function of s,

$$Y(s) = k(g(s)) = \int_0^{g(s)} \frac{1}{\sigma\sqrt{2\pi}} e^{-\frac{(g(s)-\mu)^2}{2\sigma^2}} g'(s)\mathrm{d}s \tag{4}$$

In terms of feature selection (FS), the most important goal is to select a group of the most representative features based on the original data.[22] In the mechanical stress-driven scenarios, ISC is expected to be highly dependent on the deformation of cells or the component materials. Thus, the most representative feature is the strain state of the battery that can be expressed as a strain field variable $\varepsilon(x, y, z)$, a 6D vector. Thus, without loss of generality, the argument vector $\mathbf{X}$ should be a high-dimensional

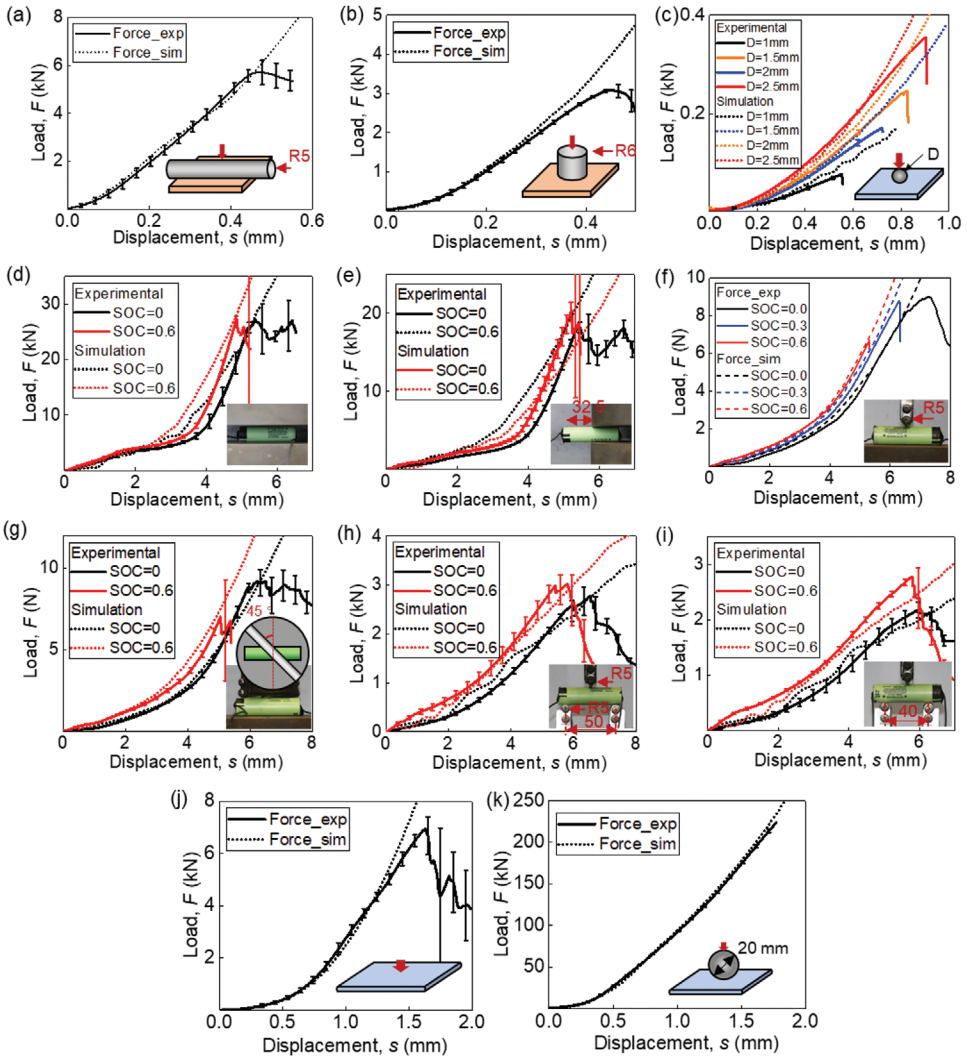

Figure 2. Experimental designs and test results. Experimental results of stacked-layer samples: a) cylinder radial indentation; b) cylinder axial indentation of cylindrical cells, and c) particle indentation of pouch cells. Experimental results of single-cell samples: d) 0%-offset compression, e) 50%-offset compression, f) 0-degree indentation, g) 45-degree indentation, h) 50 mm-span three-point bending, and i) 40 mm-span three-point bending of cylindrical cell; j) out-of-plane compression, and k) 20 mm-diameter sphere indentation of pouch cells.

vector that describes the feature of the strain state of the battery. Considering that the strain field cannot be directly obtained from experiments, the FE simulation described above is used to assist the data generation.

For a specific loading condition (Figure 3b), the strain field $\boldsymbol{\varepsilon}(x, y, z)$ of the jellyroll can also be written as the function of displacement s, that is, $\boldsymbol{\varepsilon}(x, y, z) = f(s)$, where $\boldsymbol{\varepsilon}$ is a 6D vector. The six dimensions are six strain components, that is, ε_{xx},ε_{yy},ε_{zz},ε_{xy},ε_{yz}, and ε_{zx}. According to the periodicity and continuity of the jellyroll, we ignore the position information and map the strain state $\boldsymbol{\varepsilon}(x, y, z)$ of all points (or elements) into a 6D space $\mathbf{R}^6$ (visualized by two $\mathbf{R}^3$ spaces in Figure 3b). The region formed by the mapping represents the current strain state of the jellyroll (black dot line in Figure 3b). Standardize the components by the equation:

$$\varepsilon_i' = \frac{\varepsilon_i - \varepsilon_{i,\min}}{\varepsilon_{i,\max} - \varepsilon_{i,\min}} \tag{5}$$

where $\varepsilon_{i,\min}$ is the minimum value and $\varepsilon_{i,\max}$ is the maximum value for all points (or elements), and discretize the space by a step of 0.1. The area can be expressed by a 6D matrix $\boldsymbol{\varepsilon} \rightarrow h_{ikllmn}(i,j, k, l, m, n = 0, 1, 2...10)$. It satisfies:

$$h_{ikllmn} = \begin{cases} 1, (\text{area } [i,j,k,l,m,n] \text{ is covered (red cube)}) \\ 0, (\text{area } [i,j,k,l,m,n] \text{ is not covered (blank)}) \end{cases} \tag{6}$$

$h_{ikllmn}(i,j, k, l, m, n = 0, 1, 2...10)$ is finally transferred to the argument vector $\mathbf{X}$ with a dimension of 10^6 (compress all dimensions to one dimension):

$$X(s_i) = [h_{0,0,0,0,0,0}, h_{1,0,0,0,0,0}, \ldots h_{10,0,0,0,0,0}, \ldots h_{10,10,0,0,0,0}, \ldots h_{10,10,10,10,10,10}]. \tag{7}$$

To improve calculation efficiency, we use the principal component analysis before feeding the data. Thus, along

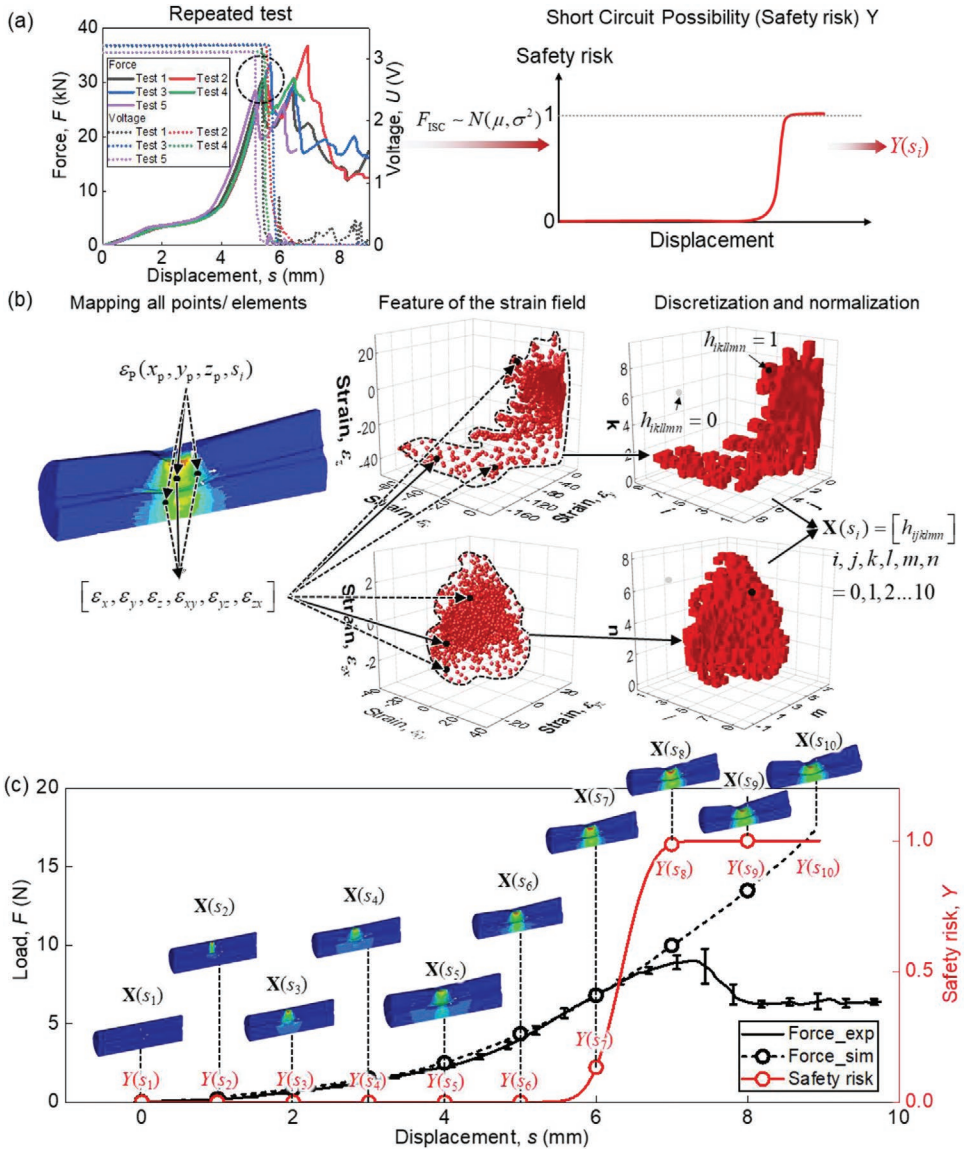

Figure 3. Generation methodology of the argument vectors and their mapping relationship. a) achievement of the safety risk *Y*, b) the generation of argument vector **X**, c) the mapping relationship between **X** and *Y*.

the force–displacement curve, several training samples can be generated, **X** and *Y* can be bridged by *s* (Figure 3c): $(\mathbf{X}_i, Y_i) = (\mathbf{X}(s_i), Y(s_i)), s_i = s_0, s_1, s_2 \ldots s_T$, where s_i can be selected as an arithmetic progression and s_T is the loading terminal displacement in simulation. The same method is also applied to other cases (Figures S3–S8), and the samples are obtained and summarized (**Table 1**).

2.2. ML Approach and Safety Risk Prediction

The safety risk prediction consists of both offline and online processes (**Figure 4**). During the offline process, the dataset is generated, and a data-driven safety risk prediction model is developed. Here, the SVR with RBF kernel from the open-source library scikit-learn is used (Supporting Information) because it is memory efficient, versatile, and effective in high dimensional spaces.[23] In the online processes, the boundary conditions and loading displacement will be input into the mechanical model. After the calculation of the FE model and the data processing, the strain state vector $\mathbf{X}_p$ is calculated and fed into the safety risk prediction model. The model then will return the safety risk Y_p. Four predictors are designed and trained to demonstrate the performance of the methodology (**Table 2**). Sixfold cross-validation is conducted to avoid over-fitting. The mean score and the standard deviation are also summarized (Table 2).

Take the indentation of the cylindrical cell, for example. The loading *F* gradually increases, and the safety risk *Y* keeps zero at first when the battery is mechanically loaded (**Figure 5**a). When the loading force or displacement is large enough, *Y* starts increasing and reaches 1 rapidly. According to the safety

Table 1. Summary of all the generated training samples.

Cell types	Sample types	Cases	Group no.	Sample numbers
Cylindrical cell	Stacked-sample	Cylinder radial direction indentation, 0%SOC	1	70
		Cylinder axial direction indentation, 0%SOC	2	70
	Cell	0%-offset radial compression, 0%SOC	3	140
		0%-offset radial compression, 60%SOC	4	140
		50%-offset radial compression, 0%SOC	5	140
		50%-offset radial compression, 60%SOC	6	140
		0-degee indentation, 0%SOC	7	180
		0-degree indentation, 30%SOC	8	180
		0-degree indentation, 60%SOC	9	180
		45-degee indentation, 0%SOC	10	180
		45-degree indentation, 60%SOC	11	180
		50 mm-span bending, 0%SOC	12	180
		50 mm-span bending, 60%SOC	13	180
		40 mm-span bending, 0%SOC	14	180
		40 mm-span bending, 60%SOC	15	180
Pouch Cell	Stacked-sample	1 mm-particle indentation, 0%SOC	16	80
		1.5 mm-particle indentation, 0%SOC	17	100
		2 mm-particle indentation, 0%SOC	18	110
		2.5 mm-particle indentation, 0%SOC	19	120
	Cell	20 mm-particle indentation, 0%SOC	20	200
		Out-of-plane compression, 0%SOC	21	220

risk, the loading process can be divided into three main stages: 1) Stage I: Low risk, safety risk close to zero, indicating almost no ISC risk; 2) Stage II: Medium risk, safety risk increases drastically with displacement/force; and 3) Stage III: High risk, ISC will probably occur. Satisfactory prediction results can be observed for both the numerical simulation model for force–displacement curves and the ML model for the safety risks. Cells under other mechanical loading conditions show a similar safety risk trend, except for the three-point bending cases (Figure 5a–c). Interestingly, the experiment showed that the ISC was not trigged upon three-point bending and the ML model is also capable of predicting the safety risk with low values, indicating no ISC will be triggered. R^2 (coefficient of determination) regression score function is employed to indicate the goodness of fit. Here, the dataset for 18 650 cylindrical cells consists of 140 training samples obtained from two stacked-layer tests, cylinder radial direction indentation (Figure S1a, Supporting Information), and cylinder axial direction indentation (Figure S1b,

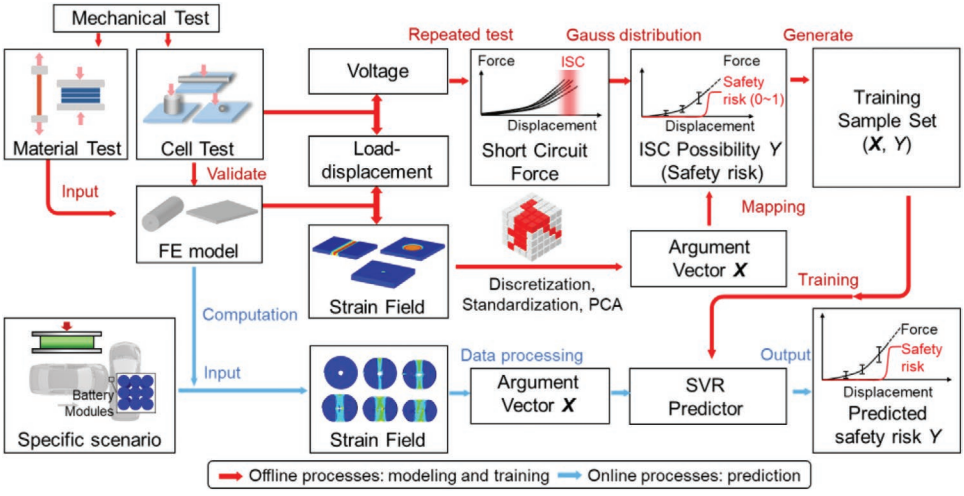

Figure 4. The flow chart of the offline training processes and the online prediction processes.

Table 2. The training/testing sample combinations and corresponding model parameters.

Predictor	Battery types	Training samples	Hyper-parameters (C, γ, ε)	Cross-validation scores (mean value, standard deviation)	Training time [s]	Testing samples
1	Cylindrical	1, 2	(1e3, 4.5e-3,1e-3)	(0.958, 0.009)	0.335	3, 7, 12
2	Pouch	16–19	(1e3, 1e-3,1e-2)	(0.933, 0.014)	1.570	20, 21
3	Cylindrical	7, 9	(5e2, 1e-5,1e-2)	(0.985, 0.004)	1.484	8
4	Cylindrical	3,4,7,9,12,13	(5e2, 1e-5,1e-2)	(0.987, 0.003)	9.545	5,6,10,11

Supporting Information). Similarly, the model for pouch cells trained by 410 samples obtained by the stacked-layer tests under several indentation loadings (Figure S5a–d, Supporting Information), also provides a satisfactory prediction of ISC risk (Figure 5d,e). These results prove the good performance and the generality of the ML modeling method to predict the safety risk of LIBs.

2.3. Generalization

In real-world engineering application scenarios, battery or vehicle designers may not have full access to the cell testing in various scenarios, for example, cells with various SOCs or upon different loading scenarios. In this case, the model established in this work can also provide a satisfactory cross-template

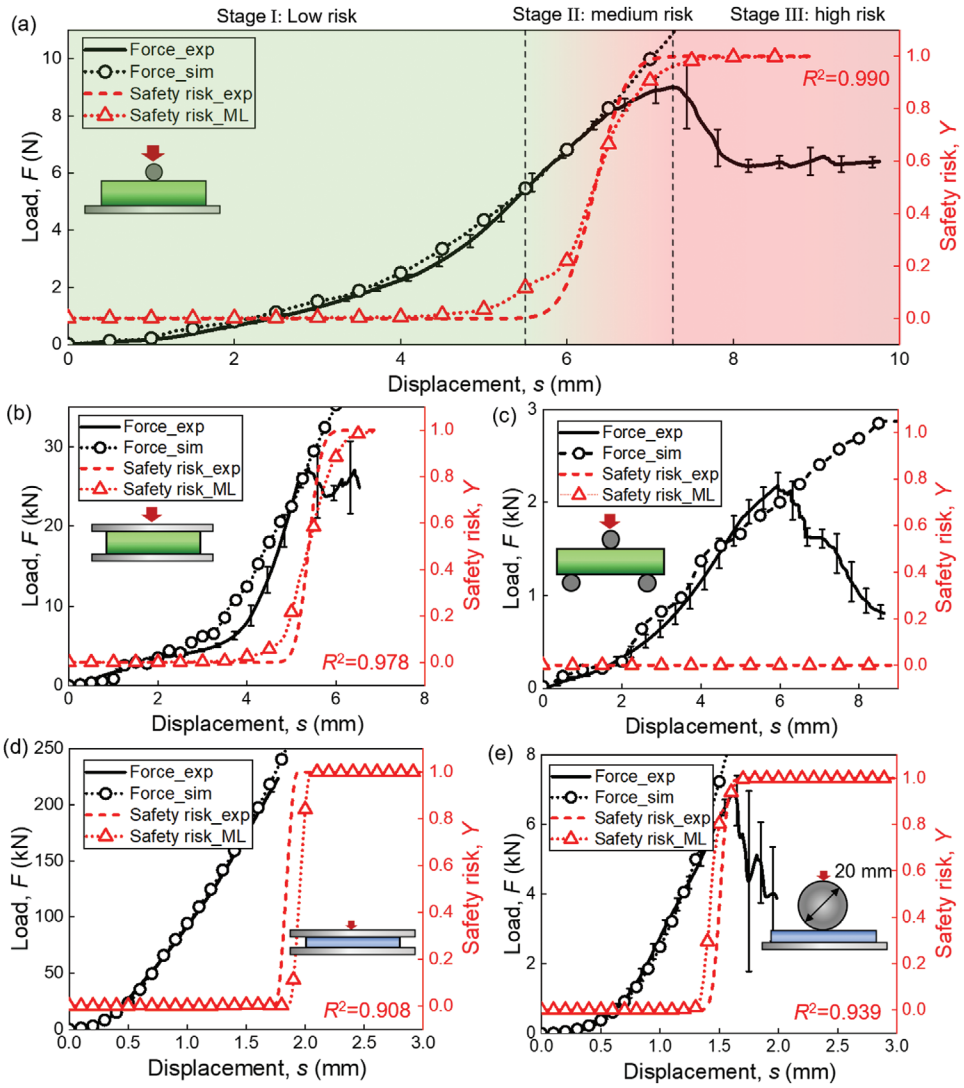

Figure 5. Safety risk evaluation of two types of cells under testing loading conditions. 18 650 cylindrical cells under a) radial compression loading, b) indentation loading, and c) three-point bending. And pouch cells under d) compression loading, and e) 20 mm-diameter sphere indentation loading.

prediction by using the results of some available cell loading tests to evaluate the safety risk of batteries with different SOCs whose safety risks are unknown such as to further facilitate battery safety status monitoring during operation.

According to some previous work, SOC of cells would have an obvious impact on the mechanical responses and ISC behaviors.[10a,b,24] The indentation tests of the cylindrical batteries also indicate that with the increase of SOC, the force response increases, and the ISC occurs earlier (**Figure 6**a). Here the results of 0%-SOC, 60%-SOC indentation tests (Figure S3a,c, Supporting Information) are used to generate the training dataset (360 samples) and then predict the safety risk of the 30%-SOC case. SOC, a real number with a value from 0 to 1, is considered as an additional feature in the input vector **X**. The yield curves are considered proportional to SOC, written as

$$\sigma_{ii} = h(\varepsilon_{ii}, SOC) = k \cdot h(\varepsilon_{ii}, SOC = 0) \tag{8}$$

where k is a constant value. The results indicate that the model provides a good interpolation prediction of the 30%-SOC case (Figure 6b).

Similarly, we can use some known loading test results to train the model and obtain an extrapolation prediction of cells under other target loading conditions. Here, the results of the 0%-offset radial compression tests (Figure S2a–b, Supporting Information) and 90-degree indentation tests (Figure S3a,c, Supporting Information) of the cylindrical cell at 0%/60% SOC is used to generate the data set and train the model (640 train samples). Then, the model is tested to evaluate the safety risk of the cells under four testing cases, 50%-offset radial compression (0%/60% SOC) (Figure 6c,d) and 45-degree indentation (0%/60% SOC) (Figure 6e,f). Results demonstrate that the model can also provide satisfactory predictions for various mechanical abuse loading scenarios (**Table 3**).

2.4. Rationalization

2.4.1. Advantages

Besides the versatility of the ML model established, a direct comparison of ISC prediction performance between the SVR predictor and a pure mechanical model based on the Mohr–Coulomb (MC) failure criterion is conducted (**Figure 7**) to demonstrate the effectiveness of the proposed model in this paper (for the sake of fairness, ML output Y here is defined as the fracture possibility). A homogenous FE model is also developed for the MC failure criterion (the same as Ref. [7e,25]). Three validation cases (training cases for the predictor, radial compression, indentation, and 50-mm three-point bending) and three testing cases (50%-offset radial compression, 45-degree indentation, and 40-mm three-point bending) are selected.

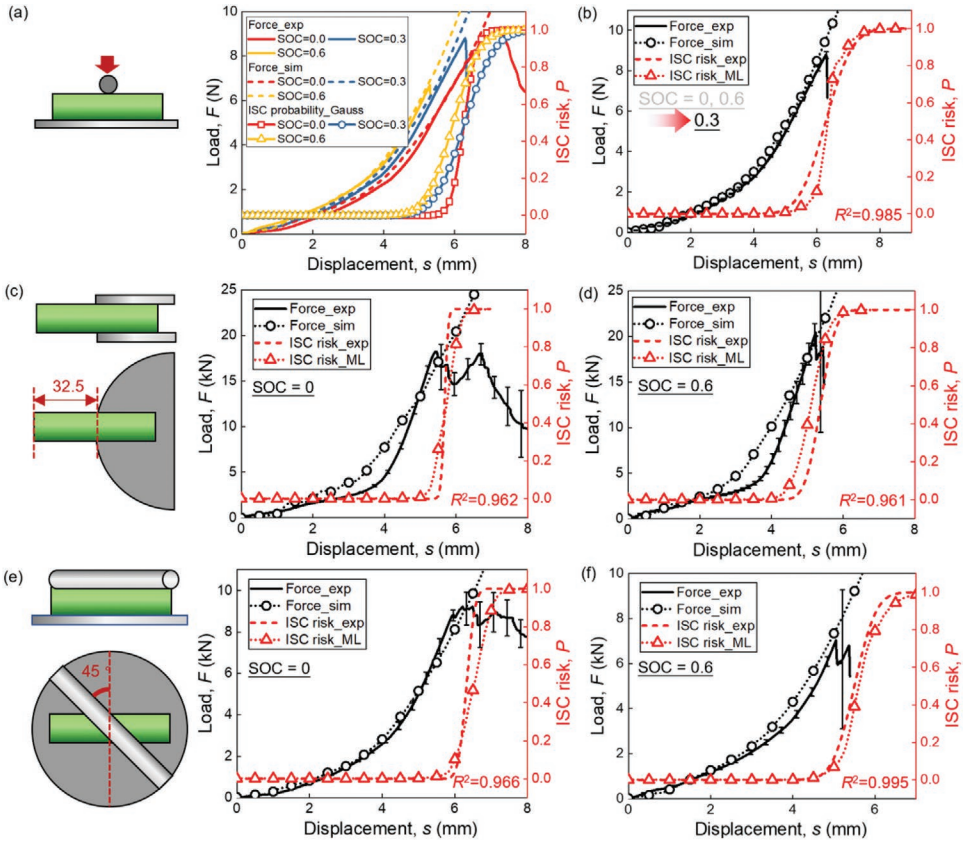

Figure 6. Safety risk prediction of cylindrical cells at different SOCs and under different loading conditions. a) Safety risks at different SOCs, b) interpolation prediction of safety risk of cells with 30%-SOC under radial compression loading. Extrapolation prediction of safety risk of cells under: 50%-offset radial compression at c) 0%-SOC and d)60%-SOC; 45-degree indentation at e) 0%-SOC and f) 60%-SOC.

Table 3. Comparisons of the ISC distance between experimental results and ML predictions.

Predictors	Test samples (group numbers)	ISC displacement [mm] (average value ± standard deviation)		Relative Error [%]
		Experiment	Simulation	
Predictor 1	3	5.39 ± 0.36	5.40 ± 0.47	0.222
	7	6.34 ± 0.48	6.35 ± 0.85	0.220
	12	–	–	–
Predictor 2	20	1.96 ± 0.07	1.84 ± 0.08	6.12
	21	1.51 ± 0.08	1.43 ± 0.10	5.30
Predictor 3	8	6.39 ± 1.04	6.35 ± 0.53	0.79
Predictor 4	5	5.68 ± 0.11	5.75 ± 0.50	1.32
	6	6.33 ± 0.26	6.60 ± 0.63	4.35
	10	5.38 ± 0.51	5.10 ± 0.60	5.12
	11	5.50 ± 0.65	5.25 ± 0.10	4.55

The homogenous FE model is validated by the three validation cases (Simulation 2 in Figure S8a–c, Supporting Information). Based on the suggested methodology in Ref. [7e], the fracture criterion (line), that is, $\sigma_1 = 0.226\sigma_3 + 0.0277$(GPa) is determined (Figure 7a). The MC criterion cannot well predict the ISC displacement of all the cases simultaneously (Figure 7b). We may notice that the MC criterion-based model can well predict Cases 2, 4, 5, but the relative errors of Cases 1, 3, 6 are huge and unacceptable. The relative errors of the MC criterion range between 10.1–35.2% for the three prediction cases and up to 36.2% for the validation cases. On the contrary, the SVR predictor not only fits the training cases very well but also provides satisfactory predictions of the unknown testing cases (Figure 7b). The relative errors are 2.5–4.3% in our model for the prediction cases and 0% difference in the validation cases. Such results from a direct comparison manifest the superiority of our model.

Previously, the ISC criteria or failure criteria is a criterion that uses a linear combination of stress-components or strain-components to predict the ISC. In this case, when the value of the function is larger than a critical value, the ISC or material failure happens. However, there is a major limitation of the traditional ways: the criterion already contains pre-set stress or strain pattern. It works well on some simple materials or structures while may not on some complicated structures like batteries. Take the MC-based ISC criterion, for example. The principal stress is calculated by the equation $\sigma_{eq} = \sigma_1 - \alpha\sigma_3$, where σ_1,σ_3 are principal stresses calculated from stress components and α is a constant.[7e,25] Considering the mechanisms of mechanically triggered ISC and limitations of traditional ISC prediction approaches, in this paper, ML method is used to substitute the criterion. Generally, the mechanically triggered ISC is produced by direct contact between anode and cathode or deformation of the separator reaches a critical state. Thus, the direct reason is the mechanical failure of deformation of the separator. Also, based on the periodical layer structure of cells, that cathode, anode, and separator are always layered together, the deformation of the separator is often corresponding to the deformation of other layers or the overall deformation of the cell. In essence, the deformation can be characterized by the intrinsic strain field of the cell. Thus, the ML features come from the transformation of the strain field of the cell at the short circuit moment.

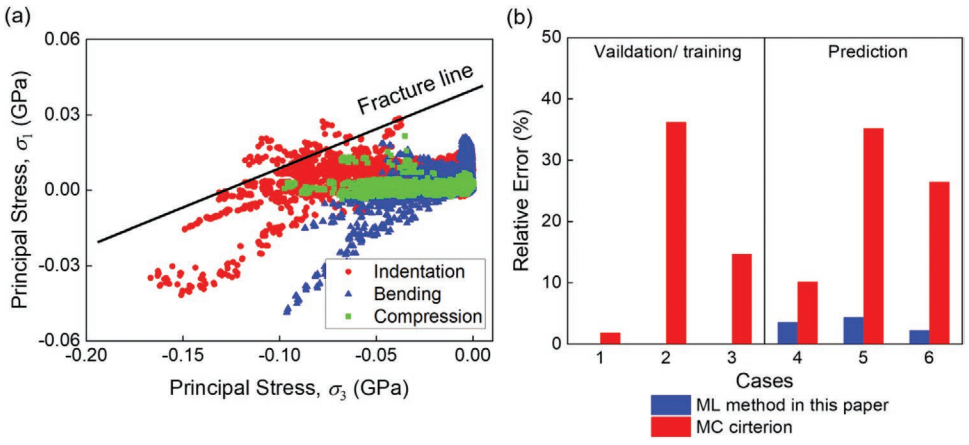

Figure 7. Comparison between the SVR predictor and the MC failure criterion. a) Determination of the fracture line. b) Comparison of ISC displacement prediction between the SVR predictor and the MC criterion (average value for experiment and the SVR predictor). Case 1: radial compression; case 2: indentation; case 3: 50-mm three-point bending; case 4: 50%-offset radial compression; case 5: 45-degree indentation; case 6: 40-mm three-point bending.

2.4.2. Pre-Conditions and Limitations

Due to the underlying principles, it is worthy to note that good performance is established based on the following pre-conditions.

(1) In the experiment design aspect, the dataset should contain samples generated from loading conditions. In the meantime, the designed mechanical tests should cover as many representative strain or stress combinations as possible, which requires a good understanding of mechanics. In this case, the model can fully capture the strain state features with a highly confident safety risk probability.
(2) In the testing sample and operation aspect, the selected sample batteries are preferable to have good uniformity, and the designed mechanical is better to have good repeatability such that the distribution of the ISC forces or the displacements can be estimated more accurately.
(3) High quality of the numerical model is necessary. We demonstrate that the RVE-based method works cost-effectively and accurately because it can significantly reduce the calculation cost while maintaining a reasonable accuracy in terms of the mechanics model computation.[19] More importantly, the RVE-based model can be more general where it can describe various battery formats using basic representative units.

In the meantime, this methodology has the following limitations:

(1) The method is only suitable for mechanically triggered ISC because we suppose that the triggering of ISC is only related to the strain state (or stress state) of the structures where the material coordinates are not be considered as features.
(2) The FE model may introduce possible modeling and computational errors, which will be further accumulated in the ML model. It is difficult for the FE model to perfectly predict the stress or strain value at each point. Thus, to avoid these errors to the greatest extent, the selected features of the ML model should be comprehensive descriptions of the strain/stress field rather than several representative points.
(3) This trained model can predict the ISC risk under mechanical loading of various types of batteries (cylindrical, pouch, and prismatic cells) with the same constituent materials. However, if the constituent materials change, the data set should also be updated accordingly.
(4) The ISC triggering under mechanical behaves in probabilistic ways for many unknown reasons, such as inconsistency of the battery samples. It is safe to use a probability to describe the ISC risk under mechanical loading only before its underlying mechanisms are clear.
(5) For future applications involving electrochemical (e.g., Li dendrite/plating, particle cracking), and thermal (e.g., separator melting) abuse caused battery safety issues, electro-chemo-mechanical models with proper criteria using intrinsic electro-chemo-mechanical features should be introduced.[7a,26] In general, the materials or structures fail when their strain states satisfy one specific or several features.

3. Conclusion

Data-driven modeling based on the prior numerical modeling is a new promising way for predicting the safety risk of LIBs with significantly reduced time-/cost-consuming and dangerous safety experiments. Here, we firstly propose the concept of safety risk since, for a complicated and highly nonlinear system like the battery, the triggering of the ISC contains stochastic factors and cannot be determined definitively. With the assist of numerical simulation and experiments, we generate a sufficient number of datasets. We then establish an ML-based model to describe and predict the ISC risk of a single cell upon mechanical abusive loading. The coefficient of determination $R^2 > 0.90$ for the entire safety risk curve for both cylindrical cells and pouch cells was observed. The relative error of the average ISC prediction is less than 6.2%. Furthermore, the generalizability of the ML-based safety risk predictor was demonstrated by extending the scenarios for cells with various SOCs and loading conditions. The success of the model manifests that the strain field should be a dominant factor for the mechanical stress-induced ISC. Our model is proven to substitute current time-consuming numerical simulation models and high-risk experiments and enables fast prediction and monitoring for possible safety risks. This work highlights the promise of combining the physical model with a data-driven model and streamlines the methodology for understanding energy storage systems.

4. Experimental Section

Mechanical Loading Tests: The quasi-static mechanical tests of the batteries were carried out with a SUNS material testing system with a 200-kN capacity (Figure S1, Supporting Information). Various platens and anvils were used to realize different loading conditions, such as platen for compression, 5 mm cylinder indenter, and different sizes of spheres (1, 1,5, 2, 2.5, 20 mm in diameter) for indentation test, and two 5 mm cylinder supporters for the bending test. Samples were placed on the corresponding supporter and applied a 100 N-preload to eliminate the possible gap between the sample and indenter. The loading speed was set as 5 mm min^{-1} for cylindrical cells and 0.5 mm min^{-1} for stacked-layer samples and pouch cells. The open-circuit voltage of the battery samples simultaneously measured by A 34 970 Agilent digital multimeter. The triggering of ISC was judged by the voltage signal (voltage decreasing). To improve the data quality, a large amount of LIB mechanical loading tests were conducted (13 scenarios, 75 tests for cylindrical cells; 6 scenarios, 30 tests for pouch cells) (**Table 4**). Thus, the experimental results cover the strain states to the largest extent.

To prepare stacked-layer samples, batteries were disassembled. The component materials, including the anode, cathode, and separator (Figure S2a, Supporting Information), were cut into squares with a dimension of 30 m × 30 mm and stacked together.

FE Simulation: The mechanical models were developed by Altair Hypermesh and solved by the nonlinear FE solver RADIOSS. Material card MAT28 was used to describe the material properties. The boundary conditions were set the same as the experimental designs. A general contact type (TYPE 7) was used to describe both the part-to-part contact and self-contact. The calculation results were presented in Supporting Information. The models can predict the force-displacement curves at various loading conditions well for both cylindrical cells and pouch cells.

The material properties of the battery components were not directly used in the finial cell model due to its high demand for computing. Here, an equivalent material property was employed for the homogenized

Table 4. Summary of the experimental setup.

Cell types	Sample types	Group number	Loading	Size or position	SOC	Loading speed
Cylindrical cell	Stacked-sample	1	Indentation	5 mm cylinder radial direction	0%	0.5 mm min^{-1}
		2	Indentation	6 mm cylinder axial direction	0%	
	Cell	3	Compression	0% (battery length) -offset, radial	0%	5 mm min^{-1}
		4		0%-offset, radial	60%	
		5		50%-offset, radial	0%	
		6		50%-offset, radial	60%	
		7	Indentation	0-degee (central axial)	0%	
		8		0-degree	30%	
		9		0-degree	60%	
		10		45-degree	0%	
		11		45-degree	60%	
		12	Bending	50 mm-span	0%	
		13		50 mm-span	60%	
		14		40 mm-span	0%	
		15		40 mm-span	60%	
Pouch Cell	Stacked-sample	16	Indentation	1 mm-particle	0%	0.5 mm min^{-1}
		17		1.5 mm-particle	0%	
		18		2 mm-particle	0%	
		19		2.5 mm-particle	0%	
	Cell	20	Indentation	20 mm-particle	0%	
		21	Compression	Out-of-plane	0%	

element according to the periodicity of the layered structure. Thus, the total element number and calculation cost were significantly reduced. The calculation times for the mechanical models are around 1 h at Intel core i7 CPU 1.80 GHz 8 cores. The FE models were validated by comparing the load-displacement curves between simulation and experimental results (Figure 2 and Figures S2–S7, Supporting Information).

ML Algorithm: The ML algorithm SVR with RBF kernel was trained to develop the data-driven safety risk prediction model (Supporting Information). To increase the model stability and reduce complexity, the data standardization and matrix dimensionality reduction were performed. Y was mapped to the range $(-\infty, +\infty)$ before feeding the data to improve the stability of the predicted curves:

$$Y' = -\ln\left(\frac{1}{Y} - 1\right) \tag{9}$$

and the predicted Y_p should be calculated by the following equation after predicting:

$$Y_p' = \frac{1}{1+e^{-Y_p}} \tag{10}$$

where Y_p is the prediction. Three hyper-parameters, C, γ, and ε, were optimized via the exhaustive grid search program. The training results and durations are listed in Table 3. The ML models were validated by comparing ISC risk-displacement curve between predictions and statistical data (Figure 5,6).

An SVM problem is a quadratic programming problem. The algorithm complexity of the QR solver was between $O(n_{\text{feature}} \times n_{\text{sample}}^2)$, and $O(n_{\text{feature}} \times n_{\text{sample}}^3)$. The computational requirements increase quicker with the number of training vectors n_{sample} rather than the feature number n_{feature}. Thus, SVMs were suitable for the ISC prediction problem because the feature number was very large while the training sample was relatively small. The time cost was trivial in the magnitude of seconds (Table 2).

Supporting Information

Supporting Information is available from the Wiley Online Library or from the author.

Acknowledgements

J.X. greatly appreciated the financial support from the U.S. Department of Energy's Office of Energy Efficiency and Renewable Energy (EERE) under the Advanced Manufacturing Office, award number DE-EE0009111.

Conflict of Interest

The authors declare no conflict of interest.

Author Contribution

Y.J.: Methodology; experiment; modeling and writing—original draft; J.L.: Experiment and data analysis; C.Y.: Experiment and data analysis; X.G.: Modeling and data analysis; W.Y.: Methodology and modeling; M.L.: Data analysis and writing—review and editing; J.X.: Conceptualization, supervision, methodology, and writing—review and editing review, and editing.

Data Availability Statement

The data that support the findings of this study are available from the corresponding author upon reasonable request.

Code Availability

Code for the modeling work is available from the corresponding author upon request.

Keywords

data-driven, lithium-ion batteries, modeling, safety risks

Received: December 14, 2020
Revised: March 4, 2021
Published online:

[1] A. Manthiram, *Nat. Commun.* **2020**, *11*, 1550.
[2] J. Wang, S. Li, Q. Zhao, C. Song, Z. Xue, *Adv. Funct. Mater.* **2020**, 2008208, https://doi.org/10.1002/adfm.202008208.
[3] P. Lyu, X. Liu, J. Qu, J. Zhao, Y. Huo, Z. Qu, Z. Rao, *Energy Storage Mater.* **2020**, *31*, 195.
[4] a) X. Zhang, E. Sahraei, K. Wang, *Sci. Rep.* **2016**, *6*, 32578; b) R. Zhao, J. Liu, J. Gu, *Appl. Energy* **2016**, *173*, 29; c) P. T. Coman, E. C. Darcy, C. T. Veje, R. E. White, *J. Electrochem. Soc.* **2017**, *164*, A587; d) B. Liu, Y. Jia, J. Li, S. Yin, C. Yuan, Z. Hu, L. Wang, Y. Li, J. Xu, *J. Mater. Chem. A* **2018**, *6*, 21475; e) S. Abada, G. Marlair, A. Lecocq, M. Petit, V. Sauvant-Moynot, F. Huet, *J. Power Sources* **2016**, *306*, 178.
[5] a) Q. Wang, P. Ping, X. Zhao, G. Chu, J. Sun, C. Chen, *J. Power Sources* **2012**, *208*, 210; b) X. Feng, M. Fang, X. He, M. Ouyang, L. Lu, H. Wang, M. Zhang, *J. Power Sources* **2014**, *255*, 294.
[6] a) P. Huang, P. Ping, K. Li, H. Chen, Q. Wang, J. Wen, J. Sun, *Appl. Energy* **2016**, *183*, 659; b) F. Larsson, J. Anderson, P. Andersson, B. E. Mellander, *J. Electrochem. Soc.* **2016**, *163*, A2854; c) X. Liu, D. Ren, H. Hsu, X. Feng, G.-L. Xu, M. Zhuang, H. Gao, L. Lu, X. Han, Z. Chu, J. Li, X. He, K. Amine, M. Ouyang, *Joule* **2018**, *2*, 2047; d) X. Feng, M. Ouyang, X. Liu, L. Lu, Y. Xia, X. He, *Energy Storage Mater.* **2018**, *10*, 246.
[7] a) Y. Jia, B. Liu, Z. Hong, S. Yin, D. P. Finegan, J. Xu, *J. Mater. Chem. A* **2020**, *8*, 12472; b) J. Xu, L. Wang, J. Guan, S. Yin, *Mater. Des.* **2016**, *95*, 319; c) E. Sahraei, M. Kahn, J. Meier, T. Wierzbicki, *RSC Adv.* **2015**, *5*, 80369; d) T. Wierzbicki, E. Sahraei, *J. Power Sources* **2013**, *241*, 467; e) L. Greve, C. Fehrenbach, *J. Power Sources* **2012**, *214*, 377.
[8] a) H. Wu, D. Zhuo, D. Kong, Y. Cui, *Nat. Commun.* **2014**, *5*, 5193; b) P. Bai, J. Li, F. R. Brushett, M. Z. Bazant, *Energy Environ. Sci.* **2016**, *9*, 3221.
[9] a) J. Weng, X. Yang, D. Ouyang, M. Chen, G. Zhang, J. Wang, *Appl. Energy* **2019**, *255*, 113761; b) D. Ouyang, J. Weng, J. Hu, M. Chen, Q. Huang, J. Wang, *Thermochim. Acta* **2019**, *676*, 205.
[10] a) J. Xu, Y. Jia, B. Liu, H. Zhao, H. Yu, J. Li, S. Yin, *Exp. Mech.* **2018**, *58*, 633; b) J. Xu, B. H. Liu, D. Y. Hu, *Sci. Rep.* **2016**, *6*, 21829; c) I. Avdeev, M. Gilaki, *J. Power Sources* **2014**, *271*, 382; d) J. Zhu, X. Zhang, E. Sahraei, T. Wierzbicki, *J. Power Sources* **2016**, *336*, 332.
[11] a) W.-J. Lai, M. Y. Ali, J. Pan, *J. Power Sources* **2014**, *248*, 789; b) C. Yuan, L. Wang, S. Yin, J. Xu, *J. Power Sources* **2020**, *467*, 228360; c) L. Wang, S. Yin, J. Xu, *J. Power Sources* **2019**, *413*, 284; d) J. Xu, B. H. Liu, X. Y. Wang, D. Y. Hu, *Appl. Energy* **2016**, *172*, 180.
[12] a) D. P. Finegan, B. Tjaden, T. M. M. Heenan, R. Jervis, M. D. Michiel, A. Rack, G. Hinds, D. J. L. Brett, P. R. Shearing, *J. Electrochem. Soc.* **2017**, *164*, A3285; b) W. Zhao, G. Luo, C.-Y. Wang, *J. Electrochem. Soc.* **2015**, *162*, A207.
[13] a) D. P. Finegan, E. Darcy, M. Keyser, B. Tjaden, T. M. M. Heenan, R. Jervis, J. J. Bailey, R. Malik, N. T. Vo, O. V. Magdysyuk, R. Atwood, M. Drakopoulos, M. DiMichiel, A. Rack, G. Hinds, D. J. L. Brett, P. R. Shearing, *Energy Environ. Sci.* **2017**, *10*, 1377; b) D. P. Finegan, J. Darst, W. Walker, Q. Li, C. Yang, R. Jervis, T. M. M. Heenan, J. Hack, J. C. Thomas, A. Rack, D. J. L. Brett, P. R. Shearing, M. Keyser, E. Darcy, *J. Power Sources* **2019**, *417*, 29.
[14] a) J. Deng, C. Bae, J. Marcicki, A. Masias, T. Miller, *Nat. Energy* **2018**, *3*, 261; b) J. Zhu, W. Li, T. Wierzbicki, Y. Xia, J. Harding, *Int. J. Plast.* **2019**, *121*, 293.
[15] a) A. Naha, A. Khandelwal, S. Agarwal, P. Tagade, K. S. Hariharan, A. Kaushik, A. Yadu, S. M. Kolake, S. Han, B. Oh, *Sci. Rep.* **2020**, *10*, 1301; b) Y. Zhang, Q. Tang, Y. Zhang, J. Wang, U. Stimming, A. A. Lee, *Nat. Commun.* **2020**, *11*, 1706; c) K. A. Severson, P. M. Attia, N. Jin, N. Perkins, B. Jiang, Z. Yang, M. H. Chen, M. Aykol, P. K. Herring, D. Fraggedakis, M. Z. Bazant, S. J. Harris, W. C. Chueh, R. D. Braatz, *Nat. Energy* **2019**, *4*, 383; d) S. Shi, J. Gao, Y. Liu, Y. Zhao, Q. Wu, W. Ju, C. Ouyang, R. Xiao, *Chin. Phys. B* **2016**, *25*, 018212; e) Y. Liu, B. Guo, X. Zou, Y. Li, S. Shi, *Energy Storage Mater.* **2020**, *31*, 434.
[16] W. Li, J. Zhu, Y. Xia, M. B. Gorji, T. Wierzbicki, *Joule* **2019**, *3*, 2703.
[17] P. M. Attia, A. Grover, N. Jin, K. A. Severson, T. M. Markov, Y.-H. Liao, M. H. Chen, B. Cheong, N. Perkins, Z. Yang, P. K. Herring, M. Aykol, S. J. Harris, R. D. Braatz, S. Ermon, W. C. Chueh, *Nature* **2020**, *578*, 397.
[18] D. P. Finegan, J. Zhu, X. Feng, M. Keyser, M. Ulmefors, W. Li, M. Z. Bazant, S. J. Cooper, *Joule* **2021**, *5*, 316.
[19] Y. Jia, X. Gao, J.-B. Mouillet, J.-M. Terrier, P. Lombard, J. Xu, *J. Energy Storage* **2020**, 102090.
[20] a) L. Wang, S. Yin, C. Zhang, Y. Huan, J. Xu, *J. Power Sources* **2018**, *392*, 265; b) L. Wang, S. Yin, Z. Yu, Y. Wang, T. X. Yu, J. Zhao, Z. Xie, Y. Li, J. Xu, *Mater. Des.* **2018**, *160*, 601.
[21] a) E. Sahraei, R. Hill, T. Wierzbicki, *J. Power Sources* **2012**, *201*, 307; b) C. Zhang, S. Santhanagopalan, M. A. Sprague, A. A. Pesaran, *J. Power Sources* **2015**, *290*, 102.
[22] Y. Liu, J. M. Wu, M. Avdeev, S. Q. Shi, *Adv. Theory Simul.* **2020**, *3*, 1900215.
[23] V. Kecman, in *Support Vector Machines: Theory and Applications* (Ed: L. Wang), Springer Berlin Heidelberg, Berlin **2005**, p. 1.
[24] a) Y. Jia, S. Yin, B. Liu, H. Zhao, H. Yu, J. Li, J. Xu, *Energy* **2019**, *166*, 951; b) W. Li, Y. Xia, J. Zhu, H. Luo, *J. Electrochem. Soc.* **2018**, *165*, A1537.
[25] B. Liu, Y. Jia, C. Yuan, L. Wang, X. Gao, S. Yin, J. Xu, *Energy Storage Mater.* **2020**, *24*, 85.
[26] a) Z. Hong, V. Viswanathan, *ACS Energy Lett.* **2018**, *3*, 1737; b) B. Liu, J. Xu, *ACS Appl. Energy Mater.* **2020**, *3*, 10931.